Dalton Transactions

ROYAL SOCIETY OF CHEMISTRY

PAPER

View Article Online
View Journal | View Issue

Cite this: *Dalton Trans.*, 2025, **54**, 2308

Defect-derived catalytic sites in Ce/Zr-UiO-66 for degradation of hexachlorobenzene†

Zhengyan Wang, Chenhao Yuan, Dong Yang, Mifen Cui, Jihai Tang, Zhuxiu Zhang * and Xu Qiao*

Received 22nd October 2024,
Accepted 3rd December 2024

DOI: 10.1039/d4dt02951h

rsc.li/dalton

It is of great significance to develop catalysts for the degradation of hexachlorobenzene from the industrial thermal process. In this paper, formic acid was used as a modulator to generate defect sites in Ce/Zr-UiO-66 with intrinsic Brønsted acidity. The defective formate ligands were removed through methanol–water vapor treatment to expose additional open metal sites with Lewis acidity. The intrinsic Brønsted acid sites of the resulting Ce/Zr-UiO-66-FA-P achieved a hexachlorobenzene degradation efficiency of 99.5% at 250 °C. The generated Lewis acid sites facilitated the C–C cleavage of degradation intermediates. More than 95.0% of the final products were CO_2/CO, coupled with chlorinated alkanes/alkenes, which outperformed other benchmark metal oxide catalysts. The Ce/Zr-UiO-66-FA-P catalyst maintained its catalytic activity in the model industrial flue gas and humid environment. The degradation pathway of hexachlorobenzene was tracked using *in situ* FT-IR spectra.

1. Introduction

Hexachlorobenzene (HCB) is a typical chlorinated aromatic hydrocarbon primarily originating from industrial processes such as solid waste incineration and metal smelting.[1–3] Direct discharge of HCB poses serious threats to human health and ecological environments.[4,5] Methods for degrading HCB, such as activated carbon adsorption, electron beam radiation and catalytic degradation, have been widely reported.[6–8] The catalytic degradation of HCB over transition metal oxides has attracted much attention due to its low energy consumption and high degradation efficiency.[9,10] However, the cleavage of the C–Cl bond in HCB forms excess chloride ions that poison the catalysts.[11] The by-products of chlorophenol and chlorobenzoquinone easily form highly toxic substances, such as polychlorinated dibenzo-*p*-dioxins and dibenzofurans (PCDD/FS), which can have further adverse environmental impact.[12,13]

The catalytic degradation of HCB is closely associated with the cleavage of C–C and C–Cl bonds,[12] and Lewis acid sites have been reported to be the core active sites for the cleavage of both C–C and C–Cl bonds.[14] The Lewis acids on metal oxides can also promote the activation of lattice oxygen, enhancing the oxidation performance of chlorinated organic pollutants and significantly reducing the amount of chlorinated alkane in the products.[15,16] It has been noted that metal oxides with an excess of Lewis acid sites are not desirable for HCB degradation because the generated Cl–metal moiety and Cl_2 during degradation will give rise to the formation of other toxic chlorine-containing by-products.[15] The Brønsted acid sites of metal oxides derived from surface hydroxyl groups have been reported to directly induce nucleophilic substitution between the adsorbed Cl˙ on oxygen vacancies and the H˙ that facilitates ring cleavage.[17,18] Therefore, metal oxide catalysts with both Brønsted and Lewis acid sites have been of great interest in the catalytic degradation of chlorinated organic pollutants. However, metal oxides with bifunctional Brønsted–Lewis acid sites require a higher reaction temperature (300–410 °C) to degrade HCB and other chlorinated aromatic hydrocarbons.[16] Such high reaction temperatures not only cause the desorption of chlorine ions in the form of Cl_2, but also form PCDD/Fs.[8] Therefore, it is necessary to develop metal oxide catalysts for the low-temperature catalytic degradation of HCB.

There is only one report regarding the use of Ce/Zr-UiO-66 for HCB degradation at 250 °C,[19] and this is also the only MOF for the degradation of chlorinated benzenes. Ce–Zr/UiO-66 with abundant Brønsted acid sites (μ_3-OH) in metal clusters exhibited a high HCB degradation efficiency of 95.0% at 250 °C, but the preliminary experiment showed that more than 80.0% of products were chlorinated benzenes because of every metal site with Lewis acidity being fully occupied by terephthalic acid. Although the decomposition of *N*,*N*′-dimethylformamide (DMF) at high temperatures (>120 °C) forms

State Key Laboratory of Materials-Oriented Chemical Engineering, College of Chemical Engineering, Nanjing Tech University, No. 30 Puzhunan Road, Nanjing 211816, China. E-mail: zhuxiu.zhang@njtech.edu.cn, qct@njtech.edu.cn

†Electronic supplementary information (ESI) available: PXRD patterns, ^{1}H NMR spectra, SEM images, IR spectra, TGA curves, XPS spectra and GC chromatograms. See DOI: https://doi.org/10.1039/d4dt02951h

formic acid that serves as the "defective ligand" for the substitution of terephthalic acid,[20] the number of resulting defect sites is less than 0.20 per cluster in Ce–Zr/UiO-66. In recent years, the modular nature and amenability to crystal engineering has enabled the control of pore chemistry of MOFs that in turn has facilitated target-specific catalytic properties.[21] In this context, the authors have successfully fine-tuned the coordination structure of the metal clusters of MOFs including M(OH) chains (M = Al, Fe, and Ga), M_3O (M = Al, Fe, and Cr) and $M_6O_4(OH)_4$ (M = Zr, Hf, and Ce) through monocarboxylic acids as defective ligands.[22–26] Furthermore, we have confirmed the importance of ligand removal with respect to the fine-tuning of the Lewis acidity of MOFs for task-specific catalytic reactions.[27–29]

In this contribution, we selected Ce/Zr-UiO-66 as the platform to generate defect-rich $(Ce/Zr)_6O_8$ clusters using additional formic acid to provide the defective ligands. The number of defect sites in the $(Ce/Zr)_6O_8$ cluster reached 2.65 per cluster. Most importantly, we used methanol vapor to replace the defective formic acid ligands with methoxy ligands that were subsequently replaced by terminal hydroxyl groups through water vapor treatment. The defect sites were thereby completely converted to open metal sites and terminal hydroxyl groups in the metal clusters. This post-vapor treatment was tracked using FT-IR and ^1H NMR, so that the coordination structure of defect sites in Ce/Zr-UiO-66 was characterized for the first time. The generation of open metal sites with Lewis acidity in the Ce/Zr-UiO-66-FA-P clusters not only enhanced the catalytic degradation efficiency of HCB, but also significantly improved the capability for deep oxidation degradation of HCB. In the degradation products of Ce/Zr-UiO-66-FA-P, there were only trace amounts of chlorinated alkanes/alkenes. The catalyst exhibited high stability and activity under flue gas and humid conditions and after multiple reuse.

2. Experimental

2.1. Reagents and materials

All reagents, $ZrCl_4$ (Aladdin Reagent (Shanghai) Co., Ltd, 98.0%), $CeCl_3{\cdot}7H_2O$ (Macklin Co., Ltd, 99.9%), benzene-1,4-dicarboxylic acid (Aladdin Reagent (Shanghai) Co., Ltd, 99.0%), HCB (Rhawn (Shanghai) Co., Ltd, 99.0%), cyclohexane (Aladdin Reagent (Shanghai) Co., Ltd, 99.0%), *N*,*N*-dimethylformamide (Sinopharm Chemical Reagent Co., Ltd, 99.5%), formic acid (Aladdin Reagent (Shanghai) Co., Ltd, 99.0%), acetone (Shanghai Lingfeng Chemical Reagent Co., Ltd, 99.5%), H_2O (Nanjing Tech University), D_2O (Beijing Chongxi High-Tech Incubator Co., Ltd, 99.8%), NaOH (Xilong Scientific Co., Ltd, 99.5%), and KBr (Sinopharm Chemical Reagent Co., Ltd, 99%), were used as received without further purification.

2.2. Catalyst preparation

2.2.1 Synthesis of Ce/Zr-UiO-66. $ZrCl_4$ (0.117 g, 0.500 mmol) and $CeCl_3{\cdot}7H_2O$ (0.186 g, 0.500 mmol) were dissolved in 30 mL of DMF in a 50 mL Teflon liner using ultrasound for 10 min. Benzene-1,4-dicarboxylic acid (0.167 g, 1.000 mmol) was then added to the solution and dissolved by ultrasound for ~15 min. The Teflon liner was sealed in an autoclave and kept under static conditions in a preheated oven at 120 °C for 24 h. The solids were washed with DMF (30 mL) three times in a day to remove unreacted precursors and acetone (30 mL) six times in 2 days to remove DMF. Then, the powder was activated at 120 °C under vacuum for 12 h prior to characterization and catalysis tests.

2.2.2 Synthesis of Ce/Zr-UiO-66-FA. $ZrCl_4$ (0.117 g, 0.500 mmol), $CeCl_3{\cdot}7H_2O$ (0.186 g, 0.500 mmol) and formic acid (3.8 mL) were dissolved in 30 mL of DMF in a 50 mL Teflon liner using ultrasound for 10 min. Benzene-1,4-dicarboxylic acid (0.167 g, 1.000 mmol) was then added to the solution and dissolved by ultrasound for ~15 min. The Teflon liner was sealed in an autoclave and kept under static conditions in a preheated oven at 120 °C for 24 h. The solids were washed with DMF (30 mL) three times in a day to remove unreacted precursors and acetone (30 mL) six times in 2 days to remove DMF. Then, the powder was activated at 120 °C under vacuum for 12 h prior to characterization and catalysis tests.

2.2.3 Synthesis of $Ce_xZr_{1-x}O_2$. This work used Ce/Zr-UiO-66 as the precursor, placing 0.500 g of Ce/Zr-UiO-66 into a tube furnace with air as the carrier gas at a flow rate of 20 mL min^{-1} and a heating rate of 2 °C min^{-1}. The furnace temperature was raised to 700 °C and this was maintained for 6 hours. Afterward, the furnace was allowed to cool naturally to room temperature before removing the sample from the tube furnace.

2.2.4 Post-treatment with methanol and water vapor. Experiments were carried out in a conventional laboratory once-through tubular plug-flow reactor at 150 °C and 1 bar. Ce/Zr-UiO-66-FA (50 mg) was loaded into the reactor in an argon-filled glovebox. Methanol was carried into the reactor by N_2 flowing through a bubbler in an ice-water bath with temperature controlled at 0 °C. The methanol treatment time was 24 h. After the methanol treatment, the samples were transferred to the activation station under high vacuum activation for 12 h at 150 °C. After the activation, 50 mg of the samples were taken into the reaction tube and passed through a water environment at 150 °C and 1 bar for 24 h. After this time, the samples were transferred to the activation station under high vacuum activation conditions for 12 h at 150 °C. After the activation, the samples were transferred to the glove box for subsequent experiments. The sample was labelled as Ce/Zr-UiO-66-FA-P, while the Ce/Zr-UiO-66, which was subjected to the same post-treatment, was labelled as Ce/Zr-UiO-66-P.

2.3. Characterization

Regular powder X-ray diffraction (PXRD) patterns of the MOFs were obtained using a Rigaku SmartLab 9 kW X-ray diffractometer instrument. Measurements were made over a range of $3° < 2\theta < 40°$ in 0.02° steps at a scan rate of 5° min^{-1}. Scanning electron microscopy (SEM) images were obtained using a Thermo Fisher Environmental Quattro SEM instrument. N_2 adsorption isotherms were recorded using a

Micromeritics TriStar II instrument at 77 K. The samples were heated to 120 °C under high vacuum for 12 h prior to the recording of the isotherms. The Brunauer–Emmett–Teller (BET) surface areas were calculated with the relative pressure ranging from 0.05 to 0.35. Thermal gravimetric analysis (TGA) measurements were carried out using a TA Instruments NETZSCH TG 209 F3 Tarsus TGA analyzer with an evolved gas analysis furnace. The samples in flowing O_2 were heated from 25 °C to 800 °C at a rate of 10 °C min^{-1}. Cerium content was determined using inductively coupled plasma (ICP) analysis, when 10 mg of the sample was dispersed in a solution mixture of nitric acid (1.0 mL), hydrochloric acid (4 mL) and hydrofluoric acid (200 μL), which was then heated in a water bath at 80 °C for one hour. ICP analyses were performed using a PerkinElmer OPTIMA7000DV ICP-OES. X-ray photoelectron spectroscopy (XPS) analysis was carried out at room temperature using a Thermo ESCALAB 250Xi spectrometer with a 150 W monochromatic Al K-alpha (1486.6 eV) source. Liquid ^1H NMR spectra were recorded using a Bruker Avance III 400 NMR spectrometer (400 MHz). The relaxation delay was set to 20 s to ensure that reliable integrals were obtained, allowing for the accurate determination of the relative concentrations of the molecular components. The number of scans per sample was 16. FTIR spectra of the MOF samples were recorded using a Bruker VERTEX 70v vacuum FT-IR spectrometer with spectral resolution of 2 cm^{-1}. Approximately 5.0 mg of the MOF sample was mixed with dry KBr powder and loaded in a Harrick DRIFTS cell in an argon-filled glove box. The sample cell was then transferred to the IR chamber, and IR spectra of the samples were recorded in flowing N_2 at various temperatures. Each spectrum was recorded as the average of 64 scans. The high-resolution transmission electron microscopy (HR-TEM), high-angle annular dark-field scanning transmission electron microscopy (HAADF-STEM) and energy-dispersive X-ray spectroscopy (EDS) element mapping data were collected using a JEM ARM 200F instrument with a Cs-corrector probe working at 200 kV. Raman spectra were recorded using a near-IR FT-Raman spectrometer (Bruker RFS 100/S instrument) with a CW Nd:YAG laser (λ_{ex} = 1064 nm) as the excitation source. A laser power of 50 mW was used. H_2 temperature-programmed reduction (H_2-TPR) and NH_3 temperature-programmed desorption (NH_3-TPD) were conducted using an automatic multipurpose adsorption instrument equipped with a custom-made thermal conductivity detector (TCD).

2.4. Catalytic reaction

2.4.1 Catalytic degradation reaction in air. The catalysts were loaded into a 1.5 mL glass ampule and 1 mL of cyclohexane solution containing HCB (the dosage of HCB was 20 mg g^{-1} of catalyst) was added. It was dried under high vacuum at 40 °C for 1 h. Then, it was transferred to a preheated fixed bed for 1 h catalytic degradation experiments. After the reaction, the glass ampule was taken out and allowed to cool naturally. The results were analyzed by gas chromatography, with each experiment repeated three times and each sample analyzed by gas chromatography three times, taking the average of the three results as the final result.

2.4.2 Catalytic degradation cycling reaction in the model industrial flue gas. During each cycle, the model industrial flue gas (gas composition: 200 ppm SO_2, 100 ppm NO_2, 11.0% CO_2, 9.0% O_2, and balance of N_2) was used to evaluate catalyst stability. After the first cycle, the used Ce/Zr-UiO-66-FA-P was collected and washed with acetone to remove the organic residuals. Then, the catalyst was transferred to the activation station at 120 °C under high vacuum for 12 h. The second cycle was then performed with the activated catalyst using the same experimental scheme. This paper followed the above experimental steps to conduct six catalytic HCB degradation cycling reactions. The amount of catalyst used, and the pretreatment and result analysis were consistent with that described in section 2.4.1.

2.4.3 Catalytic degradation reaction in different contents of water. During each catalytic reaction, water was introduced into the reactor *via* a steady flow of air through a bubbler within a bath heater. The bath heater was set to different temperatures in order to obtain water contents of 3 vol%, 6 vol%, 9 vol%, 12 vol%, 15 vol%, 20 vol%, 25 vol% and 30 vol%. A hygrograph instrument (Testo 480, Germany) was used to detect the water content in the air before introducing it into the reactor. Air flows with different contents of water were introduced into the reaction device through a pipeline wrapped in a heating belt. The amount of catalyst used, and the pretreatment and result analysis were consistent with that described in section 2.4.1.

2.5. Analytical methods

The HCB concentrations were determined using a Hewlett-Packard 5890 gas chromatograph with a ^{63}Ni electron-capture detector (GC/ECD). The decomposition products were identified using a gas chromatograph-mass spectrometer (GC/MS, Agilent 7890B-5977B). The generated CO_2 and CO were analyzed using an Agilent GC8890 with a gas chromatograph-thermal conductivity detector (GC/TCD).

The degradation efficiency of HCB (η(HCB)) was calculated using the following equation:

$$\eta(\mathrm{HCB}) = \frac{c(\mathrm{HCB})\mathrm{before} - c(\mathrm{HCB})\mathrm{after}}{c(\mathrm{HCB})\mathrm{before}} \times 100\%$$

where c(HCB)before is the initial HCB concentration and c(HCB)after is the HCB concentration after the reaction. The proportion of co-products (X(co-products)) and CO/CO_2 (X(CO/CO_2)) in the carbon distribution was calculated using the following equation:

$$X(\mathrm{CO/CO_2}) = \frac{c(\mathrm{CO/CO_2})\mathrm{after}}{c(\mathrm{CO_2})\mathrm{complete}} \times 100\%$$

$$X(\text{co-products}) = 1 - X(\mathrm{CO/CO_2})$$

where c(CO/CO_2)after is the ratio of CO/CO_2 after the reaction and c(CO_2)complete is the ratio of CO_2 produced by the complete oxidation degradation of HCB.

The concentrations of Cl^- and ClO^- were measured using an ion chromatography (IC) instrument (Shimadzu LC-20A, Japan), where HCl and Cl_2 were collected through bubbling the outlet gas stream into 250 mL of 0.0125 M NaOH solution for 60 min. An IC was employed to measure the amounts of ClO^- (which resulted from Cl_2) and Cl^- (which resulted from Cl_2 and HCl) in solution. The calculation formulas for the concentration of ClO^- and Cl^- are as follows:

$$c(ClO^-) = c_{IC}(ClO^-),$$

$$c(Cl^-) = c_{IC}(Cl^-) - c_{IC}(ClO^-);$$

where $c(ClO^-)$ and $c(Cl^-)$ are the concentrations of ClO^- and Cl^- in the product, and $c_{IC}(ClO^-)$ and $c_{IC}(Cl^-)$ are the concentrations of ClO^- and Cl^- in the IC.

Based upon the relevant literature reported,[8] the model for the catalytic degradation of HCB over Zr-UiO-66, Ce/Zr-UiO-66-FA-P and Ce-UiO-66 followed first-order kinetics. The first-order kinetics model is:

$$C_t = C_0 e^{-kt}$$

This formula was transformed into:

$$\mathrm{Ln}\left(\frac{C_t}{C_0}\right) = -kt$$

where C_t is the total amount of HCB residue (mmol g^{-1}) in the catalyst at time t, C_0 is the initial amount of HCB (mmol g^{-1}) in the catalyst, and k is the first-order kinetics constant (min^{-1}). Thus, a straight-line plot of $Ln(C_t/C_0)$ against t was used to determine the kinetic constant.

The formula for the reaction rate is:

$$r = kC_0$$

where r is the reaction rate (mmol $(g\ min)^{-1}$).

The activation energy (E_a) values for the catalytic degradation of HCB over Zr-UiO-66, Ce/Zr-UiO-66-FA-P and Ce-UiO-66 were calculated using a first-order Arrhenius equation:

$$k = Ae^{-\left(\frac{E_a}{RT}\right)}$$

The formula was transformed into:

$$\ln k = -\frac{E_a}{R} \times \frac{1}{T} + \ln A$$

where k is the kinetics constant (min^{-1}), E_a is the activation energy (kJ mol^{-1}), R is the gas constant, T is the reaction temperature (K), and A is the pre-exponential factor (min^{-1}). Thus, a straight-line plot of Ln k against $1000/T$ was used to determine the activation energy.

3. Results and discussion

3.1. Defective ligand substitution on metal clusters

Ce/Zr-UiO-66-FA was synthesized according to the literature.[30] Five different temperatures (80, 120, 150, 200, 250 °C) were selected for the post-treatment of Ce/Zr-UiO-66-FA. ^{1}H NMR spectra were used to determine the number of ligands in Ce/Zr-UiO-66-FA-P. As shown in Table S1,† the post-treatment of Ce/Zr-UiO-66-FA-P with methanol and water vapor at 80 and 120 °C still left formate ligands on the clusters. This indicated that methanol from vapor cannot completely replace the formate ligands on the clusters at low temperatures. When the temperature was above 150 °C, the formate ligands on the clusters were completely replaced. FT-IR spectra were used to evaluate the μ_3-OH change process of Ce/Zr-UiO-66-FA at temperatures from 150 to 350 °C (Fig. S1†). After reaching each target temperature, the sample was held at this temperature for 30 minutes before data collection. When the temperature was above 200 °C, the metal clusters of UiO-66-FA underwent a dehydration reaction in converting from $(Ce/Zr)_6(\mu_3\text{-}O)_4(\mu_3\text{-}OH)_4$ to $(Ce/Zr)_6(\mu_3\text{-}O)_5(\mu_3\text{-}OH)_2$ or $(Ce/Zr)_6(\mu_3\text{-}O)_6$. Therefore, 150 °C was selected as the reaction temperature for the post-treatment of Ce/Zr-UiO-66-FA.

FT-IR and ^{1}H NMR were used to clarify the structural evolution of the $(Ce/Zr)_6(\mu_3\text{-}O)_4(\mu_3\text{-}OH)_4$ cluster in Ce/Zr-UiO-66-FA during the post-treatment. The formate ligands within the structure were removed by the methanol from vapor, and the bands at 2875, 2862 and 2750 cm^{-1} associated with formate ligands were replaced by monodentate methoxy ligands with C–H stretching bands at 2933 and 2825 cm^{-1} in the FT-IR spectra (Fig. 1a). The replacement of formate ligands at 8.34 ppm by methoxy ligands at 3.21 ppm also appeared in the ^{1}H NMR spectra (Fig. 1b). Such results were consistent with our previous report.[31] The subsequent water vapor treatment replaced methoxy ligands with hydroxyl groups as indicated by the appearance of a peak at 3780 cm^{-1} related to terminal hydroxyl groups. The acidic character of Ce/Zr-UiO-66-FA-P was assessed by the adsorption of acetonitrile-d_3 (CD_3CN) followed by FT-IR. Fig. 1c shows the difference in the FT-IR spectra of adsorbed CD_3CN on the activated MOFs, in which three ν(CN) vibrational bands can be observed at 2299, 2272, and 2260 cm^{-1}. According to a previous report,[32] these bands can be respectively attributed to the adsorption of CD_3CN on Lewis acid sites and Brønsted acid sites and physisorption, so Ce/Zr-UiO-66-FA-P possesses Lewis and Brønsted acid sites in the clusters, while Ce/Zr-UiO-66-P only has Brønsted acid sites and a few Lewis acid sites in the clusters. The complete structural evolution route of the metal clusters of Ce/Zr-UiO-66-FA-P is illustrated in Fig. 2.

3.2. Structural characterization of Ce/Zr-UiO-66-FA-P

There was no change in the Ce/Zr-UiO-66-FA-P crystalline structure during the methanol–water vapor post-treatment (Fig. 1d), and the BET surface area of Ce/Zr-UiO-66-FA-P was comparable to that of the parent Ce/Zr-UiO-66-FA according to the N_2 sorption isotherm at 77 K (Fig. 1e and Table 1). The pore size distributions of both Ce/Zr-UiO-66-FA-P and Ce/Zr-UiO-66-FA-P featured a major pore of diameter 9.9 Å and two large pores, with diameters of 13.6 and 15.9 Å (Fig. S5†). In the HR-TEM image (Fig. S7†), the surface structure of Ce/Zr-UiO-66-FA-P shows no change after the post-treatment with methanol–water vapor. There were Ce, Zr, C, and O atoms in the EDS spectra of Ce/Zr-

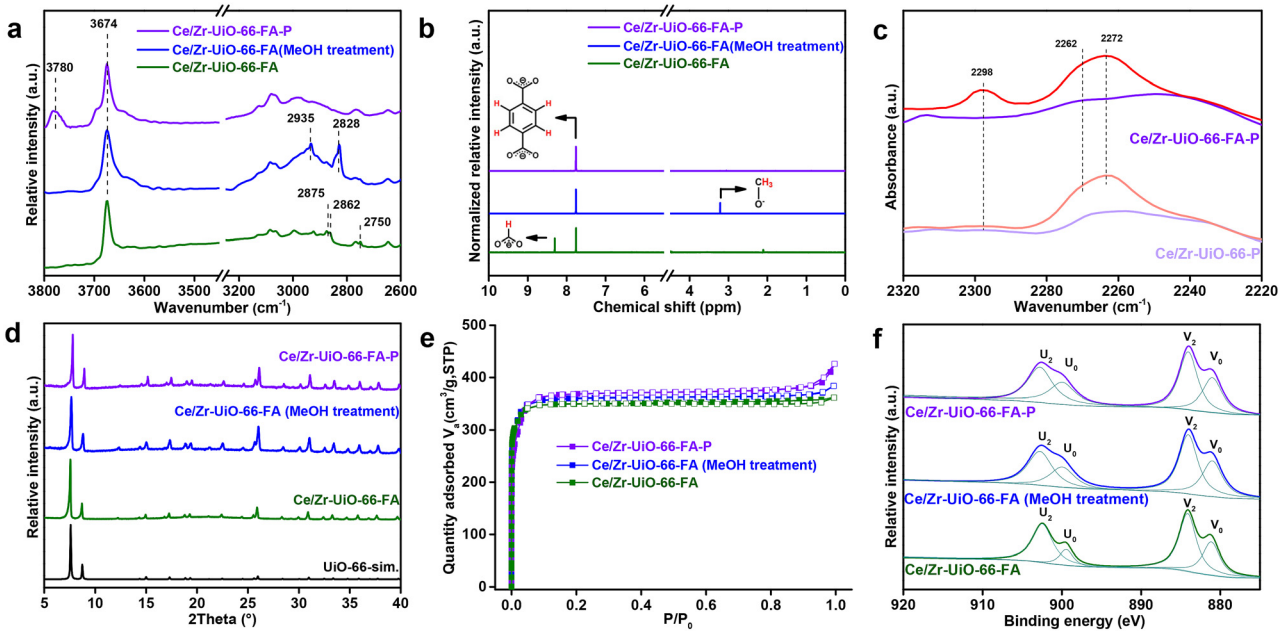

Fig. 1 (a) FT-IR spectra and (b) ^{1}H NMR spectra of Ce/Zr-UiO-66-FA, Ce/Zr-UiO-66-FA (MeOH treatment) and Ce/Zr-UiO-66-FA-P; (c) FT-IR spectra of Ce/Zr-UiO-66-P and Ce/Zr-UiO-66-FA-P before and after adsorption of CD_3CN; and (d) PXRD patterns, (e) nitrogen adsorption and desorption isotherms, and (f) Ce 3d XPS spectra of Ce/Zr-UiO-66-FA, Ce/Zr-UiO-66-FA (MeOH treatment) and Ce/Zr-UiO-66-FA-P.

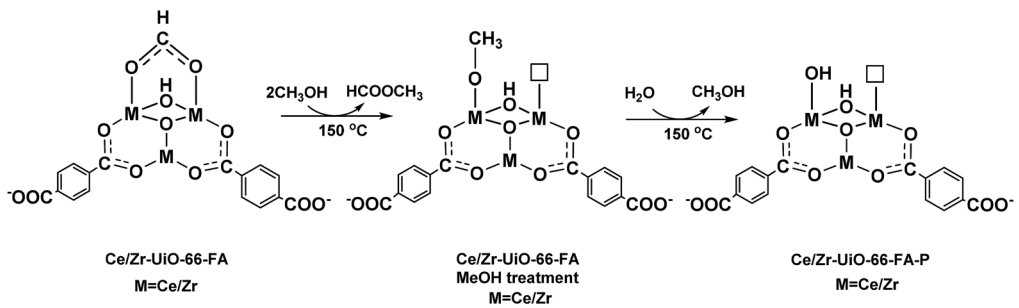

Fig. 2 Ligand changes resulting from methanol and water vapor treatment in the Ce/Zr-UiO-66-FA clusters (M = Ce/Zr).

Table 1 BET surface area, number of formate/methoxy ligands per metal cluster and Ce content for Ce/Zr-UiO-66-FA, Ce/Zr-UiO-66-FA (MeOH treatment) and Ce/Zr-UiO-66-FA-P

Samples	BET surface area ($m^2\ g^{-1}$)	Number of formate ligands per cluster	Number of methoxy ligands per cluster	Ce (wt%)	Zr (wt%)
Ce/Zr-UiO-66-FA	1329	2.69	—	4.04	29.77
Ce/Zr-UiO-66-FA (MeOH treatment)	1337	0.00	2.65	4.05	29.81
Ce/Zr-UiO-66-FA-P	1350	0.00	0.00	4.06	29.84

UiO-66-FA-P (Fig. S7†). In the HAADF-STEM and EDS element mapping of Ce/Zr-UiO-66-FA-P, the Ce, Zr, C and O atoms were uniformly distributed within the structure after the post-treatment with methanol–water vapor (Fig. S8†). The microstructure of Ce/Zr-UiO-66-FA-P did not change after post-treatment with methanol–water vapor.

The ICP results showed that the content of Ce and Zr in Ce/Zr-UiO-66-FA-P was, respectively, 4.06 wt% and 29.84 wt% (Table 1). The generation of Ce atoms in the metal clusters of Ce/Zr-UiO-66-FA-P caused a partial red shift of the $\nu(COO^-)$ symmetric stretching in the Raman spectra (Fig. S9†).[33] Thermogravimetric analysis (Fig. S2†) revealed that Ce/Zr-

UiO-66-FA-P exhibits thermal stability with 5.9% weight loss from 100 °C to 400 °C. The weight losses correspond to the loss of H_2O before decomposition. Ce/Zr-UiO-66-FA exhibits a slightly different TGA pattern, in which there is an 8.1% weight loss before 350 °C followed by a steady plateau until 430 °C before decomposition. To verify the reproducibility of the post-treatment with methanol and water vapor, five repeated experiments of the vapor treatment of Ce/Zr-UiO-66-FA were performed, and the corresponding PXRD patterns, BET surface areas and NMR spectra of all samples were consistent with each other (Fig. S3†). The formate ligands on the metal clusters were thereby shown to be completely removed (Table S2†).

The XPS spectra of Ce 3d showed the presence of a single Ce(III) valence state in Ce/Zr-UiO-66-FA-P. The peaks labelled u and v belonged to Ce $3d_{5/2}$ and Ce $3d_{3/2}$, respectively. The peaks marked at v_0 (880.2 eV), v_2 (884.3 eV), u_0 (899.2 eV) and u_2 (903.0 eV) are related to Ce(III) (Fig. 1f).[34] The valence state of Ce atoms in Ce/Zr-UiO-66-P was a mixture of Ce(III) and Ce (IV), as shown in Fig. S4e.† In Fig. S10a,† Ce/Zr-UiO-66-FA-P and Ce/Zr-UiO-66-P did not show obvious H_2 consumption peaks in the temperature range of 50–350 °C of H_2-TPR. Ce(IV) or pure cerium dioxide could be reduced to Ce(III) at 780 °C or even higher temperature.[35] However, Ce/Zr-UiO-66 had already completely collapsed at 550 °C, as shown in Fig. S2.† In order to further understand the redox activity of Ce/Zr-UiO-66-FA-P, we conducted cyclic voltammetry (CV) curve test comparisons on Ce/Zr-UiO-66-FA-P and Ce/Zr-UiO-66-P mixed with HCB. In Fig. S10b,† the reduction potentials of the mixed samples of Ce/Zr-UiO-66-FA-P with HCB and Ce/Zr-UiO-66-P with HCB are −0.81 V and −0.96 V, respectively. The oxidation potentials are −0.70 V and −0.85 V, respectively. Ce/Zr-UiO-66-FA-P has a lower electrode potential compared to that of Ce/Zr-UiO-66-P in the catalytic degradation of HCB. Therefore, Ce/Zr-UiO-66-FA-P has higher redox activity compared to Ce/Zr-UiO-66-P.

3.3. Catalytic degradation of HCB

Ce/Zr-UiO-66-FA-P, Ce/Zr-UiO-66-P and $Ce_xZr_{1-x}O_2$ were selected for catalytic degradation of HCB at different temperatures. In Fig. 3a, at a reaction temperature of 250 °C, the degradation efficiency of HCB over $Ce_xZr_{1-x}O_2$ was only 19.6%. The degradation efficiency of HCB over Ce/Zr-UiO-66-FA-P was 98.9% at 150 °C. In comparison, the degradation efficiency of HCB over Ce/Zr-UiO-66-P at 150 °C was only 80.8%. As the temperature increased, the degradation efficiency of HCB over Ce/Zr-UiO-66-P increased, and at 200 °C it reached 97.5%. When the temperature was 250 °C, both Ce/Zr-UiO-66-P and Ce/Zr-UiO-66-FA-P exhibited a degradation efficiency of 99.5% (Fig. 3a).

Although the degradation efficiency of HCB over both Ce/Zr-UiO-66-FA-P and Ce/Zr-UiO-66-P was 99.5% at 250 °C, there was a difference in carbon distribution between these two catalysts (Fig. 3b). Ce/Zr-UiO-66-P exhibited 15.9% of CO/CO_2 and 84.1% of co-products at 250 °C. The co-products were mainly pentachlorobenzene and tetrachlorobenzene according to GC-MS analysis (Fig. 4a). In contrast, the CO/CO_2 ratio increased to

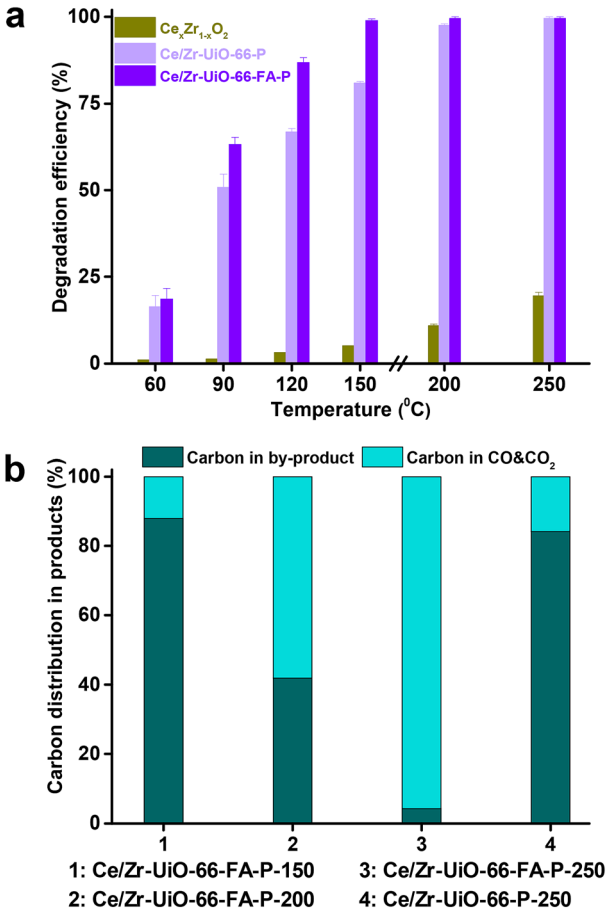

Fig. 3 (a) HCB degradation efficiency and (b) carbon distribution of the products over Ce/Zr-UiO-66-FA-P and Ce/Zr-UiO-66-P at different temperatures.

95.8% and the co-products only account for 4.2% over Ce/Zr-UiO-66-FA-P at 250 °C. The co-products were mainly comprised of small amounts of pentachlorobenzene, pentachlorophenol and chlorinated alkanes/alkenes (Fig. 4). At lower temperatures, the proportion of co-products in the carbon distribution of Ce/Zr-UiO-66-FA-P increased as the reaction temperature decreased, and 12.1% of CO/CO_2 and 87.9% of co-products were present for Ce/Zr-UiO-66-FA-P at 150 °C. These co-products were mainly pentachlorophenol, pentachlorobenzene and a small amount of tetrachlorobenzene (Fig. 4a). Therefore, the abundant amount of open metal sites with Lewis acidity in Ce/Zr-UiO-66-FA-P significantly improved the degradation efficiency and complete degradation capability of HCB compared to those of Ce/Zr-UiO-66-P. The analysis of the distribution of carbon degradation products reflected the degradation deepness of HCB and the participation of active sites.

We mixed Ce/Zr-UiO-66-FA-P with a mixed solution of HCB and cyclohexane before the catalytic degradation of HCB. After drying under high vacuum, cyclohexane was completely removed and did not participate in the catalytic degradation of HCB (Fig. S11a†). Cyclohexane is a non-polar aprotic solvent. We chose acetone (a polar aprotic solvent) and methanol

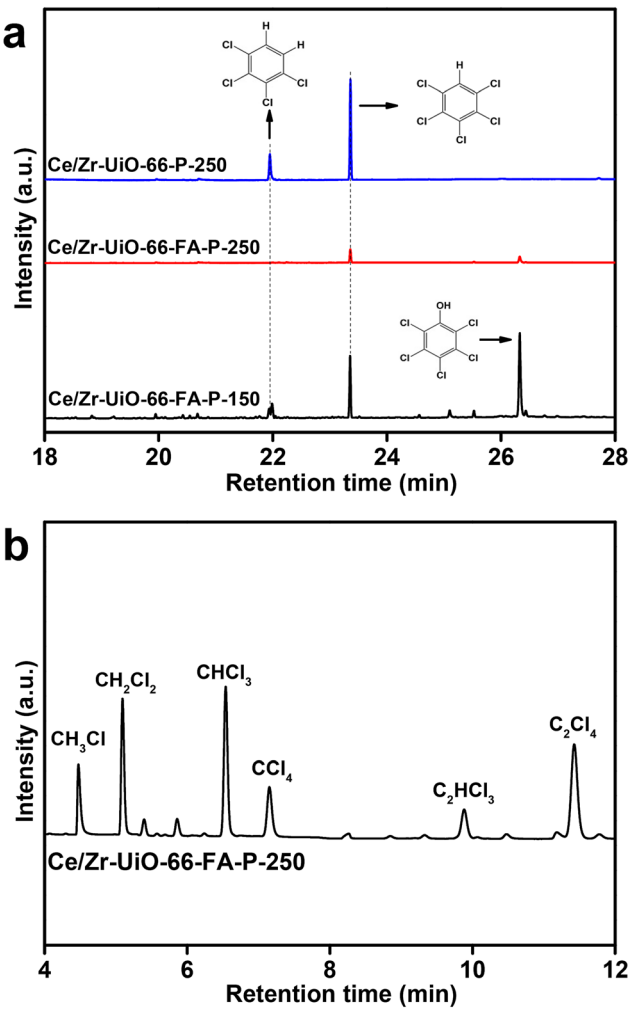

Fig. 4 Gas chromatography spectra of (a) intermediates from HCB degradation over Ce/Zr-UiO-66-P and Ce/Zr-UiO-66-FA-P at 250 °C and over Ce/Zr-UiO-66-FA-P at 150 °C and (b) chlorinated alkane/alkene products from HCB catalytic degradation over Ce/Zr-UiO-66-FA-P at 250 °C. Peak identification at different retention times was carried out through mass spectrometry.

(a polar protic solvent) for comparison to determine whether solvents with different properties have any impact on the catalytic degradation of HCB by Ce/Zr-UiO-66-FA-P. After drying under high vacuum, methanol and cyclohexane were also completely removed (Fig. S11a†). Different solvents did not affect the catalytic degradation efficiency of Ce/Zr-UiO-66-FA-P and the CO/CO_2 ratio in the carbon distribution of the products (Fig. S11c and d†). All Ce/Zr-UiO-66-FA-P samples maintained good crystalline structure after the reaction (Fig. S11b†). The reaction rate for the catalytic degradation of HCB at 250 °C also did not change (Fig. S12 and Table S5†).

Meanwhile, we added different amounts of formic acid during the synthesis to construct Ce/Zr-UiO-66 metal clusters with different numbers of open metal sites for the catalytic degradation of HCB. In Fig. S13 and Table S6,† as the number of open metal sites in the metal clusters of Ce/Zr-UiO-66 increased, the catalytic degradation efficiency of HCB at 150 °C and the ratio of CO_2/CO in the carbon distribution of the products at 250 °C also increased. The open metal sites in the Ce/Zr-UiO-66 metal clusters were positively correlated with the degradation efficiency of catalytic degradation of HCB and the CO_2/CO ratio in the carbon distribution of the products.

The results from TEM images and TGA curves (Fig. S13-1 & 4†) indicated that Ce/Zr-UiO-66-FA-P has a higher number of missing linkers and larger crystal size compared to Ce/Zr-UiO-66-P. It was not possible to independently control the number of missing linkers and crystal size through direct synthesis methods. Therefore, we used post-synthetic treatment to regulate the number of defects while maintaining the crystal sizes of Ce/Zr-UiO-66-FA-P and Ce/Zr-UiO-66-P to the greatest extent possible. In Fig. S13 and Table S7,† with the same crystal size but different number of missing linkers in the metal cluster, the total acidity of the catalysts differs by more than two times. However, with the same missing linkers in the metal cluster but different crystal sizes, the total acidity of the catalysts differs by no more than 0.2 mmol (NH_3 per g). In comparison, the number of missing linkers in the metal clusters of Ce/Zr-UiO-66 has a much greater impact on the total amount acidity of the catalyst than the crystal size. In Fig. S15,† there is a positive correlation between the efficiency of HCB degradation and the total acidity of the catalyst. The more acidity sites on the catalyst, the higher its catalytic activity for the C–Cl bond in the catalytic degradation of HCB (Table 2).

We calculated the kinetic constants for the catalytic degradation of HCB at different temperatures for Zr-UiO-66, Ce/Zr-UiO-66-FA-P and Ce-UiO-66. As calculated, the kinetic constants for these catalysts followed the sequence of Ce/Zr-UiO-66-FA-P > Zr-UiO-66 > Ce-UiO-66. Ce-UiO-66 has strong redox capability, but its structural stability is relatively poor. During the catalytic degradation of HCB, its structure continuously collapsed (Fig. S21†), reducing the removal efficiency of HCB and also the kinetic constant. In Ce/Zr-UiO-66-FA-P, the Zr atoms in the metal clusters enhanced the structural stability and combined with the strong redox of the Ce atoms. Therefore, it has a higher kinetic constant compared to Zr-UiO-66.

Fig. S17† shows the Arrhenius plots of Zr-UiO-66, Ce/Zr-UiO-66-FA-P, Ce-UiO-66, H_2BDC, $ZrCl_4$ and $Ce(NH_3)_2(NO_3)$ in the catalytic degradation of HCB. As calculated, the E_a values for these catalysts follow the sequence of H_2BDC > $ZrCl_4$ > $Ce(NH_3)_2(NO_3)$ > Zr-UiO-66 > Ce/Zr-UiO-66-FA-P > Ce-UiO-66, as

Table 2 Kinetic constants for the catalytic degradation of HCB over Zr-UiO-66, Ce/Zr-UiO-66-FA-P and Ce-UiO-66

	Kinetic constant (k) (min^{-1})			
Samples	120 °C	150 °C	200 °C	250 °C
Zr-UiO-66	0.019	0.031	0.043	0.068
Ce/Zr-UiO-66-FA-P	0.027	0.049	0.065	0.077
Ce-UiO-66	0.016	0.017	0.018	0.020

shown in Table 3. All MOF catalysts have lower E_a values for the catalytic degradation of HCB compared to metal salts and linkers. Ce-UiO-66 required the lowest activation energy in the catalytic degradation of HCB. However, its structure has completely collapsed after the reaction (Fig. S21†), and the removal efficiency of HCB over Ce-UiO-66 was no more than 60% (Fig. S20†). In Ce/Zr-UiO-66-FA-P, the addition of Zr atoms to the metal clusters increased its structural stability and combined with the strong redox of Ce atoms. The activation energy required for the reaction was lower than that of Zr-UiO-66.

The catalytic properties of Ce/Zr-UiO-66-FA-P were compared with those of six metal oxides (SrO_2/Fe_2O_3,[12] SrO_2/Fe_2O_3,[12] $Ca_2Fe_2O_5$,[36] $Cu_xMg_{1-x}Al_2O_4$,[13] V_2O_5-WO_3/TiO_2,[9] and γ-Al_2O_3[10]) and six MOFs (Zr-UiO-66,[37] Ce-UiO-66,[38] Zr-MOF-808,[39] Zr-hcp UiO-66,[24] Al-MIL-53,[40] and Ti-MIL-125[41]) in the context of HCB degradation efficiency and its carbon distribution. The experiments for all samples were conducted under the same conditions as those of Ce/Zr-UiO-66-FA-P for the catalytic degradation of HCB. The efficiencies for the catalytic degradation of HCB by the six metal oxides were 85.6%, 93.5%, 82.8%, 85.7%, 93.1%, and 80.1% at 250 °C (Fig. S21a†). The efficiencies of HCB degradation over six metal oxide catalysts at 250 °C were lower than the efficiency of HCB degradation over Ce/Zr-UiO-66-FA-P. The efficiencies of catalytic degradation of HCB over six MOFs were 96.5%, 53.6%, 59.5%, 50.3%, 89.6%, and 45.7% at 250 °C (Fig. S21b†). Only Zr-UiO-66 and Al-MIL-53 have degradation efficiencies that exceed 80.0% at 250 °C. The efficiencies of degradation of HCB over other MOFs were all below 60.0% at 250 °C. The PXRD patterns indicated the structural collapse of Ce-UiO-66, Zr-MOF-808, Zr-hcp UiO-66, and Ti-MIL-125 after the catalytic degradation of HCB (Fig. S22†).

The ratio of CO/CO_2 for V_2O_5-WO_3/TiO_2 was the highest at 35.7%, while the ratio of CO/CO_2 for other metal oxides was less than 20.0% in the carbon distribution (Fig. S23a†). Among these metal oxides, alkaline metals exhibited strong hydrodechlorination performance. However, the active sites on metal oxides were often occupied by chloride ions, which led to catalyst poisoning and deactivation at lower temperatures. In the carbon distribution of Zr-UiO-66 and Al-MIL-53, the ratio of CO/CO_2 was less than 1.0% (Fig. S23b†). For Zr-UiO-66 and Al-MIL-53, the metal clusters have sufficient Brønsted acid sites to provide a hydrogen source for the hydrodechlorination reaction, thereby exhibiting high efficiency in HCB degradation. However, the metal clusters lacked sufficient Lewis acid sites, resulting in a very low proportion of product from the oxidation reaction.

We chose three benchmarked redox catalysts (V_2O_5, CeO_2, and MnO_x) and three benchmarked acid catalysts (H-ZSM-5, H–Y and H-BETA) for comparison with Ce/Zr-UiO-66-FA-P in the catalytic degradation of HCB. All samples were assessed under the same conditions as those of Ce/Zr-UiO-66-FA-P for the catalytic degradation of HCB. The efficiencies of catalytic degradation of HCB over V_2O_5, CeO_2 and MnO_x were 39.1%, 50.9% and 42.4% at 250 °C (Fig. S23a†). The ratio of CO/CO_2 for V_2O_5 was the highest at 14.5%, while the ratio of CO/CO_2 for other metal oxides was less than 15% in the carbon distribution (Fig. S23b†). Among these metal oxides, alkaline metals exhibited strong hydrodechlorination performance. However, the active sites on metal oxides were often occupied by chloride ions, which led to catalyst poisoning and deactivation.

The efficiencies of catalytic degradation of HCB over H-ZSM-5, H–Y and H-BETA were 96.8%, 96.9% and 96.1% at 250 °C (Fig. S23a†). The ratio of CO/CO_2 was less than 5.0% in the carbon distribution (Fig. S23b†). The catalysts have sufficient OH groups to provide a hydrogen source for the hydrodechlorination reaction, thereby exhibiting high efficiency in HCB degradation. However, the catalysts lacked sufficient Lewis acid sites, resulting in a very low proportion of product from the oxidation reaction.

3.4. Catalytic stability study of Ce/Zr-UiO-66-FA-P

The flue gas generated from the incineration of solid waste usually contains a lot of acid gases such as NO_2 and SO_2, which might induce the deactivation of the catalyst. In Fig. 5a, the model industrial flue gas (gas composition: 200 ppm SO_2, 100 ppm NO_2, 11% CO_2, 9% O_2, and balance of N_2) was used to evaluate catalyst stability, and HCB degradation efficiency remained above 90.0% after six cycles. The water resistance of the catalyst was then evaluated by using humid air with water content of 3–30 vol%. In Fig. 5b, there was no change in HCB degradation efficiency until the water content increases to 9 vol%. When the water content was 30 vol%, the HCB degradation efficiency was less than 60.0%. Excess water molecules have been reported to cover the active sites, resulting in a decrease in the efficiency of degradation of HCB.

We conducted comprehensive characterization studies of the Ce/Zr-UiO-66-FA-P catalyst after the stability test. From the PXRD patterns (Fig. S24a†), Ce/Zr-UiO-66-FA-P maintained good crystalline structure after the reaction. The BET surface area and pore structure of Ce/Zr-UiO-66-FA-P did not change after the reaction (Fig. S24b, c and Table S9†). The terminal hydroxyl groups (3780 cm^{-1}) and μ_3-OH (3674 cm^{-1}) signals of Ce/Zr-UiO-66-FA-P remained consistent with those peak values before the reaction, as shown in the FT-IR spectra (Fig. S24d†). The structure of the metal clusters in Ce-UiO-66-FA-P remained unchanged after the reaction. The number of defect sites in the metal clusters was not changed after the reaction (Table S9†). Meanwhile, we determined the carbon distribution of the products over Ce/Zr-UiO-66-FA-P in the catalyst

Table 3 E_a value for the catalytic degradation of HCB over Zr-UiO-66, Ce/Zr-UiO-66-FA-P, Ce-UiO-66, H_2BDC, $ZrCl_4$ and $Ce(NH_3)_2(NO_3)$

Samples	E_a (kJ mol^{-1})
Zr-UiO-66	17.46
Ce/Zr-UiO-66-FA-P	16.62
Ce-UiO-66	3.69
H_2BDC	30.09
$ZrCl_4$	26.27
$Ce(NH_3)_2(NO_3)$	25.27

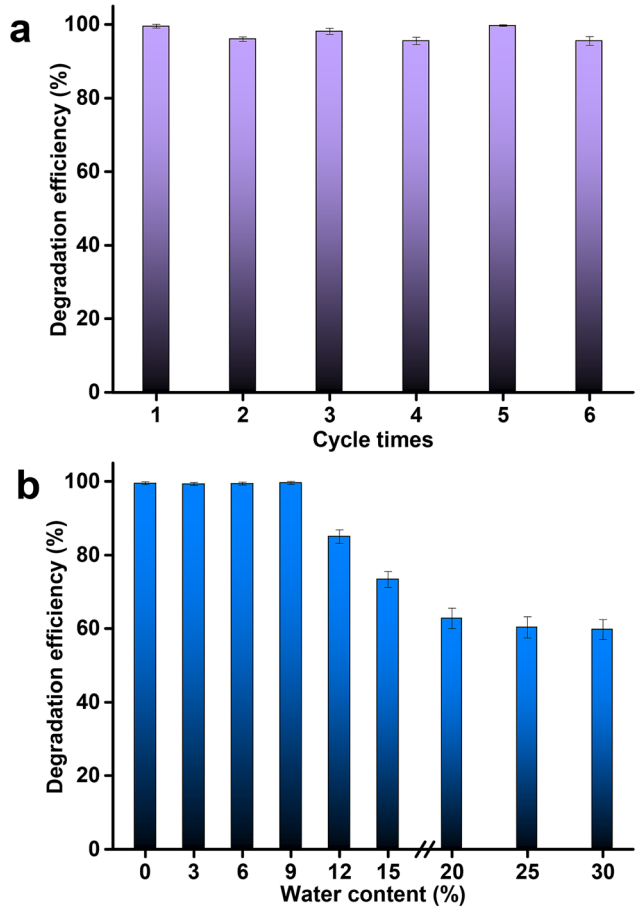

Fig. 5 (a) Efficiency of catalytic degradation of HCB in the model industrial flue gas over Ce/Zr-UiO-66-FA-P for six reaction cycles at 250 °C. (b) Efficiency of catalytic degradation of HCB with different contents of water at 250 °C.

stability test. The ratio of CO/CO_2 was more than 90% for the catalytic degradation of HCB over Ce/Zr-UiO-66-FA-P at 250 °C in the model industrial flue gas with 6 cycling reactions and different contents of water (3 vol%, 6 vol% and 9 vol%) (Fig. S25†). Then, we conducted six additional cycling reactions for the catalytic degradation of HCB over Ce/Zr-UiO-66-FA-P in the model industrial flue gas at 250 °C. In Fig. S26,† the efficiency of catalytic degradation of HCB fluctuated between 90 and 95% over six reaction cycles and Ce/Zr-UiO-66-FA-P maintained extremely high catalytic activity during the cycling reactions.

Finally, we tested inorganic chloride in the products. In Table 4, the distribution of inorganic chloride in the products was primarily in the form of HCl, with only a minimal amount of Cl_2. The reason was that the oxygen clusters of Ce/Zr-UiO-66-FA-P were rich in μ_3-OH and terminal hydroxyl groups, providing an abundant hydrogen source to induce HCl production. In addition, the lower reaction temperature also prevented the occurrence of the Deacon reaction during the oxidation process of HCB.[18]

Table 4 Concentrations of HCl and Cl_2 in the products at 250 °C

	HCl (ppm)	Cl_2 (ppm)
Ce/Zr-UiO-66-FA-P in air	206.81	4.61
Ce/Zr-UiO-66-FA-P in the model industrial flue gas	188.55	4.99
Ce/Zr-UiO-66-FA-P in 9% water content	238.41	3.78

3.5. Degradation pathway

After the post-treatment, there are abundant Brønsted acid sites and open metal sites with Lewis acidity in the metal clusters of Ce/Zr-UiO-66-FA-P. It has been reported that Brønsted acid sites serve as hydrogen sources to convert chloride ions to HCl in the catalytic degradation of HCB.[19] However, the role of open metal sites and bridging oxygen in the $(Ce/Zr)_6O_8$ cluster has not been reported in the catalytic degradation of HCB. To address this problem, *in situ* diffuse reflectance infrared Fourier transform spectroscopy was used to track the HCB degradation process over Ce/Zr-UiO-66-FA-P. Ce/Zr-UiO-66-P with rare defect sites was selected for comparison. In each experiment, the catalyst was mixed with HCB at a mass ratio of 25 : 1. The reaction was performed at three reaction tempera-

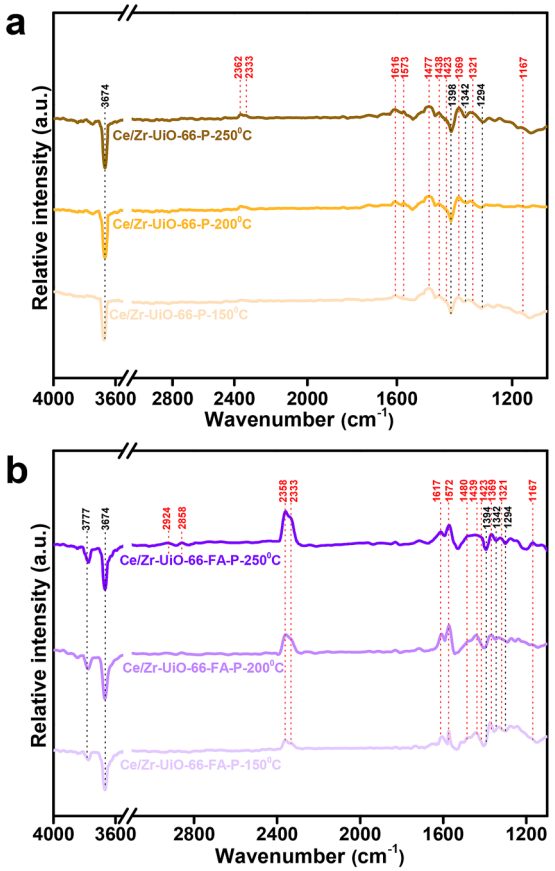

Fig. 6 *In situ* DRIFTS spectra of HCB degradation catalyzed over Ce/Zr-UiO-66-P (a) and Ce/Zr-UiO-66-FA-P (b) at 150, 200 and 250 °C.

tures of 150, 200 and 250 °C with an air flow of 10 mL min^{-1}. The FT-IR spectra were recorded every 30 minutes during the test.

The Ce content in Ce/Zr-UiO-66-FA-P was 4.06 wt% according to the ICP test. According to the literature,[42] when the Ce element content is less than 17 wt%, the metal clusters of Ce/Zr-UiO-66 exist in the forms of $Zr_6(\mu_3\text{-}O)_4(\mu_3\text{-}OH)_4(COO)_{12}$ and $CeZr_5(\mu_3\text{-}O)_4(\mu_3\text{-}OH)_4(COO)_{12}$. According to the Ce 3d XPS results, the Ce atoms in the Ce/Zr-UiO-66-FA-P metal cluster exhibited a single Ce(III) valence state, so that there was one oxygen vacancy in the cluster to form $Ce^{III}Zr_5(\mu_3\text{-}O)_3(\mu_3\text{-}OH)_4(COO)_{12}$. To maintain the charge balance, a μ_3-OH group occupies such an oxygen vacancy to form $Ce^{III}Zr_5(\mu_3\text{-}O)_3(\mu_3\text{-}OH)_5(COO)_{12}$.[30] Meanwhile, there are 2.65 defect sites in each metal cluster of Ce/Zr-UiO-66-FA, a value that is consistent with 3 terminal hydroxyl groups after post-treatment. Therefore, the Ce/Zr cluster of Ce/Zr-UiO-66-FA-P is $Ce^{III}Zr_5(\mu_3\text{-}O)_3(\mu_3\text{-}OH)_5(COO)_9(OH)_3$.

The FT-IR spectrum of the HCB–catalyst mixture recorded at room temperature was used as the background for subsequent tests. The functional groups related to FT-IR are highly consistent with the results of carbon distribution (Fig. 3b) and gas chromatography (Fig. 4) of the products in HCB degradation over Ce/Zr-UiO-66-FA-P and Ce/Zr-UiO-66-P. In Fig. 6a, the negative band at 1398 cm^{-1} corresponds to the C–Cl bond in HCB, while the negative bands at 1342 and 1294 cm^{-1} correspond to the stretching vibrations of the C=C bond in the aromatic ring of HCB. All these negative bands indicate HCB degradation over Ce/Zr-UiO-66-P. The negative peak at 3674 cm^{-1} showed the interaction between HCB and μ_3-OH during the catalytic degradation of HCB. Such interaction was closely associated with the adsorption and activation of HCB.[15] According to the research by Su *et al.*, the hydrodechlorination reaction is divided into two steps:[43] the first step is the adsorption of HCB on Brønsted acid sites (μ_3-OH) to form an aryl anion by obtaining two electrons respectively from two Ce(III) ions (stage 1(ii) in Fig. 7); the next step is the protonation of the aryl anion by μ_3-OH groups to form chlorinated benzenes (stage 1(iii) in Fig. 7). The change of Ce valence was confirmed by the Ce 3d XPS spectra of Ce/Zr-UiO-66-FA-P. The valence state of Ce atoms in the as-synthesized Ce/Zr-UiO-66-FA-P was Ce(III), and it became a mixture of Ce(III) and Ce(IV) after 30 minutes of reaction (Fig. S27†). As a result, as shown in Fig. 6a, the bands at 1477, 1423, 1369 and 1321 cm^{-1} can be ascribed to the stretching vibrations of the C=C moieties of pentachlorobenzene and tetrachlorobenzene. The presence of pentachlorobenzene and tetrachlorobenzene was also confirmed by the GC-MS data (Fig. 4a). Moreover, such a reaction process is consistent with the spectra of reported defect-free Ce/Zr-UiO-66 with only Brønsted acid sites.[19]

In Fig. 6b, the abovementioned hydrodechlorination reaction also occurred over Ce/Zr-UiO-66-FA-P because of the presence of Brønsted acid sites in Ce/Zr-UiO-66-FA-P. It is noted

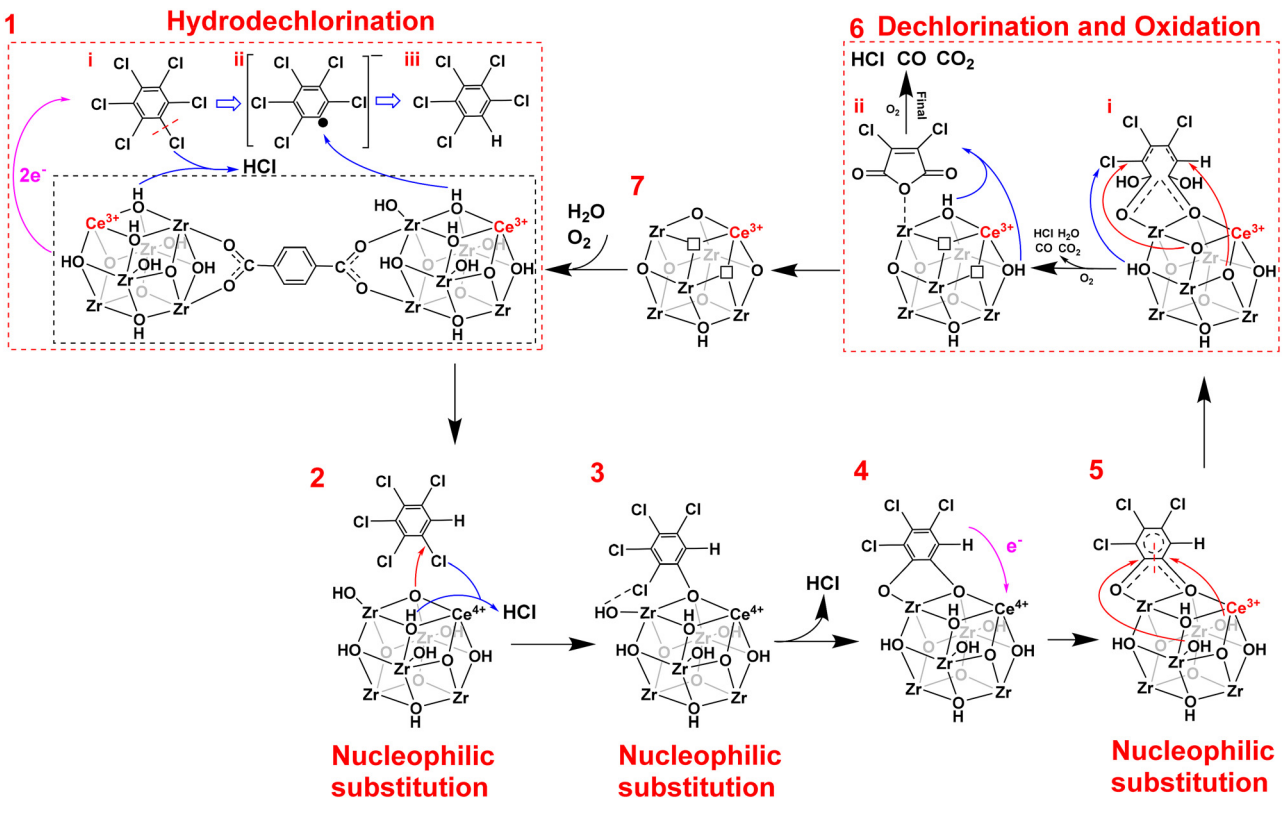

Fig. 7 Proposed degradation pathway of HCB over the Ce/Zr-UiO-66-FA-P catalyst.

that the open metal sites and bridging oxygen triggered the oxidation reaction, and pentachlorobenzene degradation was selected as the example to explore oxidation pathways (Fig. 7). The Cl group of pentachlorobenzene adsorbed at the open Ce atom and then the C–Cl bond underwent a nucleophilic attack with μ_3-O to form a chlorophenol intermediate confirmed by the bands at 1572 and 1439 cm^{-1} assigned to the C=C stretching vibrations of phenol species (stage 2 in Fig. 7).[36] The subsequent nucleophilic substitution occurred on this chlorophenol intermediate by the adjacent terminal OH group (negative peak at 3777 cm^{-1}) to produce pyrocatechol species (stage 3 in Fig. 7) that were confirmed by the band at 1617 cm^{-1}.[15] Then the electron transfer between the pyrocatechol species and the metal cluster formed a π-conjugated system as the transition state (stage 4 in Fig. 7). The C–O bonds in such conjugated systems were attacked by another two terminal hydroxyl groups to break the C–C bond in the benzene ring (stage 5 in Fig. 7).[44] Then, the remaining μ_3-OH moieties in the metal cluster continued to undergo similar nucleophilic substitution reactions with remaining C–Cl bonds, and meanwhile, the remaining μ_3-O^{2-} oxidized the C–H group (stage 6(i) in Fig. 7). This step produced chlorinated maleic anhydride (band at 1167 cm^{-1}) as the main product and $CO/CO_2/H_2O$/HCl as the co-products.[45] Similar dechlorination and oxidation continued to occur on chlorinated maleic anhydride to eventually form CO/CO_2 (bands at 2358 and 2333 cm^{-1}) and HCl (stage 6(ii) in Fig. 7). Meanwhile, the weak peaks that appeared at 2924 and 2858 cm^{-1} were ascribed to chlorinated alkanes/alkenes derived from the oxidative cleavage of chlorinated maleic anhydride,[17,18] and these results were also consistent with those of GC-MS (Fig. 4b). Finally, all the oxygen vacancies, μ_3-O^{2-} sites and terminal hydroxyl groups were recovered by H_2O and O_2 in air (stage 7 in Fig. 7). In contrast, the Ce/Zr-UiO-66-P clusters have only a small number of open metal sites with Lewis acidity, so there are only weak peaks of pyrocatechol species (band at 1616 cm^{-1}), chlorophenol species (bands at 1573 and 1438 cm^{-1}), chloride maleic anhydride (band at 1167 cm^{-1}) and CO_2 (bands at 2362 and 2333 cm^{-1}).

4. Conclusions

In this work, formic acid was used as a modulator to generate defect sites in Ce/Zr-UiO-66. The post-treatment with methanol and water vapour successfully removes the defective formate ligands to generate Lewis acid sites. The resulting Ce/Zr-UiO-66-FA-P catalyst has Brønsted–Lewis bifunctional sites and showed an HCB degradation efficiency of 95.8% at 250 °C. The degradation products have only a small amount of chlorinated alkanes/alkenes. The Ce/Zr-UiO-66-FA-P catalyst maintains high reaction activity and stability for the model industrial flue gas after six catalytic cycles. Under conditions of a humid environment (water content 9%), Ce/Zr-UiO-66-FA-P also maintained high reaction activity. The abundant μ_3-OH and terminal OH groups converted inorganic chloride to HCl instead of Cl_2.

Only a few MOFs have been found to maintain high catalyst stability in the catalytic degradation of HCB. The strong acidity of HCl generated during catalytic degradation can easily decompose the structure of these MOFs. Therefore, exploring MOFs with high chemical stability for degradation of chlorinated aromatic pollutants is important. Defects in MOFs have diverse structures that are closely associated with different reaction pathways in terms of HCB degradation. So far, only UiO-66 was selected as the platform to explore the structure–property correlation. Recent studies have shown that the vacancy sites within the metal clusters can also serve as potential active sites for catalytic reactions. The development of new active sites in the metal clusters of MOFs and the synergistic effects between various active sites to catalyze the degradation of pollutants is of great importance for exploring new pathways and structure–activity relationships.

Author contributions

Zhengyan Wang: data curation, methodology, formal analysis, and writing. Chenhao Yuan: data curation, methodology, and formal analysis. Dong Yang: conceptualization, supervision, and funding acquisition. Mifen Cui: funding acquisition. Jihai Tang: writing – review & editing. Xu Qiao: supervision and funding acquisition. Zhuxiu Zhang: conceptualization, supervision, and funding acquisition.

Data availability

The data that support the findings of this study are available from the corresponding author upon reasonable request.

Conflicts of interest

There are no conflicts to declare.

Acknowledgements

This study was supported by funding from the National Key Research and Development Program (2023YFC3905401, Z. Z.), the National Natural Science Foundation of China (22072066, D.Y), the "Distinguished Professor" program (2018) of Jiangsu province and the Priority Academic Program Development of Jiangsu Higher Education Institutions (PAPD), and the Key R&D Program of Jangsu Province (BE2021710, Xu Qiao).

References

1 J. L. Barber, A. J. Sweetman, D. van Wijk and K. C. Jones, *Sci. Total Environ.*, 2005, **349**, 1–44.
2 A. Grochowalski and J. Konieczynski, *Chemosphere*, 2008, **73**, 97–103.

3 T. Ba, M. Zheng, B. Zhang, W. Liu, G. Su and K. Xiao, *J. Environ. Monit.*, 2009, **11**, 867–872.
4 A. S. Randi, C. Cocca, V. Carbone, M. Nuñez, M. Croci, A. Gutiérrez, R. Bergoc and D. L. K. de Pisarev, *Toxicol. Sci.*, 2006, **89**, 83–92.
5 Y. Zhang, Z. Ma, X. Xie, D. Wu, X. Peng and J. Li, *Chemosphere*, 2023, **336**, 139254–139254.
6 Y. Gao, H. Zhang and J. Chen, *Chemosphere*, 2010, **81**, 1012–1017.
7 Y. Xiao, J. Jiang, Y. Yang and G. Gao, *Chem. Eng. J.*, 2011, **173**, 415–421.
8 J. Chen, D. Zhong, H. Hou, C. Li, J. Yang, H. Zhou, L. Hu and L. Wang, *Chem. Eng. J.*, 2016, **294**, 246–253.
9 Y. Yang, G. Yu, S. Deng, S. Wang, Z. Xu, J. Huang and B. Wang, *Chem. Eng. J.*, 2012, **192**, 284–291.
10 L. Zhanga, M. Zhenga, B. Zhang and G. Su, *Environ. Technol.*, 2012, **33**, 1945–1951.
11 J. Zhao, W. Xi, C. Tu, Q. Dai and X. Wang, *Appl. Catal., B*, 2020, **263**, 118237.
12 G. Su, Y. Liu, L. Huang, Y. Shi, A. Zhang, L. Zhang, W. Liu, L. Gao and M. Zheng, *Chemosphere*, 2013, **90**, 103–111.
13 Y. Fan, X. Lu, Y. Ni, H. Zhang, M. Zhu, Y. Li and J. Chen, *Appl. Catal., B*, 2011, **101**, 606–612.
14 X. Weng, P. Sun, Y. Long, Q. Meng and Z. Wu, *Environ. Sci. Technol.*, 2017, **51**, 8057–8066.
15 X. Lv, S. Cai, J. Chen, D. Yan, M. Jiang, J. Chen and H. Jia, *Catal. Sci. Technol.*, 2021, **11**, 4581–4595.
16 Q. Dai, J. Wu, W. Deng, J. Hu, Q. Wu, L. Guo, W. Sun, W. Zhan and X. Wang, *Appl. Catal., B*, 2019, **249**, 9–18.
17 S. Bai, Q. Dai, X. Chu and X. Wang, *RSC Adv.*, 2016, **6**, 52564–52574.
18 P. Sun, W. Wang, X. Dai, X. Weng and Z. Wu, *Appl. Catal., B*, 2016, **198**, 389–397.
19 Y. Fan, H. Zhang, M. Ren, Y. Zhang, Y. Li, L. Wang and J. Chen, *Chem. Eng. J.*, 2021, **414**, 128782.
20 R. Wei, C. A. Gaggioli, G. Li, T. Islamoglu, Z. Zhang, P. Yu, O. K. Farha, C. J. Cramer, L. Gagliardi, D. Yang and B. C. Gates, *Chem. Mater.*, 2019, **31**, 1655–1663.
21 J. J. Perry, J. A. Perman and M. J. Zaworotko, *Chem. Soc. Rev.*, 2009, **38**, 1400–1417.
22 D. Yang, M. Babucci, W. H. Casey and B. C. Gates, *ACS Cent. Sci.*, 2020, **6**, 1523–1533.
23 D. Yang and B. C. Gates, *ACS Catal.*, 2019, **9**, 1779–1798.
24 D. Yang and B. C. Gates, *J. Phys. Chem. C*, 2024, **128**, 8551–8559.
25 D. Yang and B. C. Gates, *Adv. Mater.*, 2024, **36**, e2305611.
26 D. Yang and B. C. Gates, *Acc. Chem. Res.*, 2021, **54**, 1982–1991.
27 Z. Wang, M. Babucci, Y. Zhang, Y. Wen, L. Peng, B. Yang, B. C. Gates and D. Yang, *ACS Appl. Mater. Interfaces*, 2020, **12**, 53537–53546.
28 S. Zhuang, H. Huang, Y. Xiao, Z. Zhang, J. Tang, B. C. Gates and D. Yang, *J. Catal.*, 2021, **404**, 128–138.
29 X. Chen, Y. Lyu, Z. Wang, X. Qiao, B. C. Gates and D. Yang, *ACS Catal.*, 2020, **10**, 2906–2914.
30 M. Ronda-Lloret, I. Pellicer-Carreno, A. Grau-Atienza, R. Boada, S. Diaz-Moreno, J. Narciso-Romero, J. C. Serrano-Ruiz, A. Sepulveda-Escribano and E. V. Ramos-Fernandez, *Adv. Funct. Mater.*, 2021, **31**, 202102582.
31 D. Yang, C. A. Gaggioli, D. Ray, M. Babucci, L. Gagliardi and B. C. Gates, *J. Am. Chem. Soc.*, 2020, **142**, 8044–8056.
32 X. Feng, J. Hajek, H. S. Jena, G. Wang, S. K. P. Veerapandian, R. Morent, N. De Geyter, K. Leyssens, A. E. J. Hoffman, V. Meynen, C. Marquez, D. E. De Vos, V. Van Speybroeck, K. Leus and P. Van Der Voort, *J. Am. Chem. Soc.*, 2020, **142**, 3174–3183.
33 S. Bercha, S. Rathod, O. Zavorotynska and S. M. Chavan, *ACS Omega*, 2024, **9**, 44321–44335.
34 W. Cai, F. Chen, X. Shen, L. Chen and J. Zhang, *Appl. Catal., B*, 2010, **101**, 160–168.
35 Y. Cui, L. Xu, M. Chen, X. Lian, C.-e. Wu, B. Yang, Z. Miao, F. Wang and X. Hu, *Catal. Sci. Technol.*, 2019, **9**, 5605–5625.
36 X. Ma, H. Sun, H. He and M. Zheng, *Catal. Lett.*, 2007, **119**, 142–147.
37 N. Aljammal, J. Lauwaert, B. Biesemans, T. Vandevyvere, M. K. Sabbe, P. M. Heynderickx and J. W. Thybaut, *J. Catal.*, 2024, **433**, 115471.
38 H. Molavi and M. S. Salimi, *Langmuir*, 2023, **39**, 17798–17807.
39 G. Ye, L. Wan, Q. Zhang, H. Liu, J. Zhou, L. Wu, X. Zeng, H. Wang, X. Chen and J. Wang, *Inorg. Chem.*, 2023, **62**, 4248–4259.
40 J. X. Li, S. Zhang, Y. M. Hua, Y. C. Lin, X. Wen, E. Mijowska, T. Tang, X. C. Chen and R. S. Ruoff, *Green Energy Environ.*, 2024, **9**, 1138–1150.
41 K. Yuan, Z. Y. Liu, Z. Yan, Q. B. Yun, T. Q. Song, J. Guo, X. T. Zhang, D. C. Zhong, Z. Y. Tang, T. B. Lu and W. P. Hu, *Angew. Chem., Int. Ed.*, 2024, **63**, e202402693.
42 K. A. Lomachenko, J. Jacobsen, A. L. Bugaev, C. Atzori, F. Bonino, S. Bordiga, N. Stock and C. Lamberti, *J. Am. Chem. Soc.*, 2018, **140**, 17379–17383.
43 G. J. Su, H. J. Lu, L. X. Zhang, A. Q. Zhang, L. Y. Huang, S. Liu, L. W. Li and M. H. Zheng, *Environ. Sci. Technol.*, 2014, **48**, 6899–6908.
44 N. Li, X. Xing, J. Cheng, Z. Zhang and Z. Hao, *J. Hazard. Mater.*, 2021, **403**, 123952.
45 J. Lichtenberger and M. D. Amiridis, *J. Catal.*, 2004, **223**, 296–308.